Ocean Dynamics (2021) 71:175–194
https://doi.org/10.1007/s10236-020-01440-x

Multi-scale variability of circulation in the Gulf of Tonkin from remote sensing of surface currents by high-frequency radars

Manh Cuong Tran[1,2,3] · Alexei Sentchev[1] · Kim Cuong Nguyen[3]

Received: 8 June 2020 / Accepted: 28 December 2020 / Published online: 8 January 2021

Abstract

The sea surface velocity measurements obtained during the period of 2014–2016 using two high-frequency radars (HFR), which were installed on the northern coast of Vietnam, were reprocessed by using a variational approach (EOF/2dVar) to provide an extended dataset. The high temporal resolution of measurements and large spatial coverage of the radar data enabled the assessment of the surface circulation in the data-poor region of the southern Gulf of Tonkin (GoT) and the characterization of its temporal variations in a wide range of scales: from tidal frequency to annual cycle. It was found that tidal motions account for a large percentage (approximately 60%) of surface current variability in the GoT. The temporal variability of the kinetic energy of the surface currents is tightly correlated with wind variations in the monsoon-dominated atmospheric circulation system. Stratification, induced by the discharge of the Red River, also affects the tidal currents within the coastal region (~ 40 km wide) by modifying the tidal ellipses polarizations. Close to the shore, the prominent coastal flow experiences large temporal variations in response to wind and buoyancy forcing. The seasonal variability of the zonal wind component was found to play a significant role in coastal flow speed variations through the cross-shore mass exchange. The Red River freshwater discharge controls the seaward extension of the coastal flow and causes asymmetry in the seasonal variability of flow velocity. The data obtained and analysis results could be useful for the improvement of the regional circulation models, for further studies of the physical and biological processes in the GoT, and for marine resource management.

Keywords HF radar · Gulf of Tonkin · Surface circulation · Multi-scale variability

1 Introduction

In recent years, the land-based high-frequency oceanographic radars (known as HF radar or "HFR") have been extensively used to monitor surface currents in numerous coastal areas. The HFR observing systems, which are capable of providing information on both the spatial and temporal variabilities of ocean currents within the top few meters, are largely used in oceanographic research and coastal water management. Datasets from HFR observations for the last two decades have enabled a better understanding of the physical processes in nearshore waters and significant advances in the study of the coastal ocean. For example, Bassin et al. (2005) analyzed the HFR data and demonstrated that the bottom-generated vorticity acts on the prevailing westward current on the inner shelf of the Southern California Bight and supplies nutrients to the shallow water zones via the cross-shore transport. Using the data obtained from two mooring sites and the HFR measurements, Yoshikawa et al. (2007) evaluated the wind-driven flow and estimated the Ekman transport through the Tsushima Strait. On the basis of the HFR observations, extreme complexity and variability of the surface circulation in two tide-dominated regions (The English Channel and Iroise Sea) have been revealed by Sentchev et al. (2009, 2013), Thiébaut and Sentchev (2017). In the Iroise Sea, which is characterized by powerful tidal motions with velocities exceeding 3 m s^{-1}, high waves, and wind, the HFR provides a unique possibility for current monitoring (Sentchev et al. 2013). Recently, HFR measurements were obtained from the Alderney Race (Channel Islands region), where the tidal

Responsible Editor: Pierre De Mey-Frémaux

✉ Kim Cuong Nguyen
cuongnk@hus.edu.vn

[1] Laboratory of Oceanology and Geosciences, CNRS UMR 8187, Univ. Littoral Côte d'Opale, Univ. Lille, IRD, 62930 Wimereux, France

[2] Center for Oceanography (CFO), Vietnam Administration of Seas and Islands (VASI), 8 Phao Dai Lang, Dong Da, Hanoi, Vietnam

[3] VNU University of Science, Vietnam National University, 334 Nguyen Trai, Thanh Xuan, Hanoi, Vietnam

current velocity is among the largest in the world (in excess of 5 m s^{-1}) (Lopez et al. 2020). HFR measurements have been used to assess the local hydrodynamics, tidal stream resource variability, and wave-current interaction prior to the deployment of tidal energy converters in this region (Furgerot et al. 2020).

With the rapid development of sea-based activities in Asian countries (including marine transportation, fishery, and harbor constructions), the demand for near real-time observation has increased in recent decades, particularly along the western Pacific Ocean periphery. This led to the development of HFR-based observation networks in numerous Asian countries, such as Taiwan, South Korea, Japan, and the Philippines (Fujii et al. 2013). The Gulf of Tonkin (hereafter referred to as the GoT), which is a shallow semi-enclosed marginal sea located in the northwestern Vietnam East Sea (internationally known as the South China Sea or SCS), is one of the regions where monitoring of such currents by the HFR has been conducted since 2012. This highly populated, tourist-attractive region is exposed to a wide range of natural and anthropogenic risks. For instance, the northern sector of Vietnam and the GoT are often affected by tropical storms every year (IMHEN and UNDP 2015). In recent decades, several powerful typhoons, i.e., Wutip (September 25 to October 1, 2013) and Doksuri (September 10–16, 2017), swept through the region and caused significant damages to the coastal areas. Furthermore, the area is exposed to risks related to climate change. In this region, the sea level is expected to increase by about 0.6 m at the end of this century, which results in the inundation of about 5.9% of the coastal areas in the Red River delta (IMHEN and UNDP 2015). The increase in rain and storm intensities can also result in more frequent flooding, higher storm surges, land erosion, etc. Besides, an extreme hazardous event in the GoT caused by human activities occurred during mid-2016. Toxin waste, which was illegally discharged from the Formosa steel factory (Vung Ang Economic zone near the XUAN radar site) to the seawater, caused severe degradation of the marine environment and heavily impacted the fishing and tourism industry in four central provinces of Vietnam. Due to the potential natural and anthropogenic risks, a robust environmental monitoring network, and, to a great extent, better knowledge of the hydrodynamic processes are important to promote sustainable development.

Despite its privileged geographic location and economic importance, the GoT attracted a few oceanography studies. The general features of the GoT circulation have often been deduced from larger scale studies of SCS dynamics (Wyrtki 1961; Gan et al. 2006; Chern et al. 2010). In the previous studies focusing on the dynamics of the GoT (Ye and Robinson 1983); Manh and Yanagi 2000; Ding et al. 2013; Gao et al. 2013, 2015), tides and wind were found to be the dominant factors controlling the regional circulation. The tidal dynamics of the GoT have been studied since the 1960s and have been fairly well documented by Wyrtki (1961), who identified the role of four main tidal constituents (K1, O1, M2, and S2) in the tidal regime of the SCS. During the 1980s, Ye and Robinson (1983) explored the contribution of K1 and M2 tidal constituents to the water dynamics in the GoT using their two-dimensional nonlinear hydrodynamic model. More recently, the major characteristics and variability of the tidal currents in this region were assessed by Ding et al. (2013) using the Global-FVCOM model. Nguyen et al. (2014) explored the resonance of the diurnal tides in the GoT using the high-resolution numerical model (ROMS at 1/25°). Piton et al. (2020) used the flexible mesh model (T-UGOm) to demonstrate the influence of the model bathymetry and the bottom shear stress parameterization on the simulation accuracy of the tidal dynamics in the GoT. These studies have provided an overview of the tidal dominant processes. In addition, the effects of seasonal wind on the current pattern have been documented in the modeling studies of Manh and Yanagi (2000), Ding et al. (2013), and Gao et al. (2015) and confirmed that the wind plays a significant role in the current variability in the GoT. These studies provided insight into the understanding of the dominant physical processes and mechanisms that govern the large-scale circulation.

However, the model-based studies mentioned above were insufficient to fully characterize the circulation in the GoT and investigate the mechanisms that govern its variability. First, the studies were often focused on a particular physical process or a single time period. Thus, the inputs were often idealized, i.e., homogeneous density, climatological forcing, and the neglect of riverine freshwater discharge with an inaccurate coastal bathymetric dataset. In the most recent modeling study, Piton et al. (2020) addressed a key challenge in the simulation of the tidal dynamics of the GoT as the complex topography and particularly in the shallow water zone. The lack of available observations in the area prevents a detailed characterization of the circulation and model validation. The first systematic survey of the gulf was conducted by China and Vietnam in the early 1960s and was followed years later by several sparse surveys, which were often limited to the northern and eastern sides of the GoT (Gao et al. 2017). The circulation pattern in the GoT, especially in summer (gulf-scale cyclonic or anti-cyclonic), still remains a topic of debate. Numerous scientists, such as Liu and Yu (1980) and Manh and Yanagi (2000), reported that the wind-induced current is the most important component of the circulation and that the pattern of the surface current in summer is anti-cyclonic. However, other researchers believe that the density-driven current significantly contributes to and strongly affects the circulation of the GoT in summer (Gao et al. 2017). Based on the data from a 1-year-long mooring dataset in the northern gulf, Ding et al. (2013) found that the sub-tidal current is highly correlated with the surface wind in winter but not in summer. This suggests that the anti-cyclonic pattern of wind-driven circulation in the GoT is not realistic. Gao et al. (2015) analyzed the current structures in the GoT using the POM model and reported that in summer, the circulation in the northern part is cyclonic and is mostly being driven by the wind stress curl, whereas in the southern part, the circulation is anti-cyclonic and is largely affected by the SCS water intrusion. In the modeling study, Rogowski et al. (2019) argued that the current pattern in the GoT is gulf-scaled cyclonic, even without the river input. The controversy in the characterization of the circulation of the GoT often comes from the lack of recent field measurements, mostly in the western section of the gulf. Remote sensing of the currents at a large scale of the gulf by HFR seems particularly suitable for the investigation of the water dynamics of the GoT.

Rogowski et al. (2019), who combined the HFR measurements, satellite altimetry, ocean color data, and numerical modeling, provided insight into the seasonal variability of the circulation in the GoT. In our study, we used the HFR observations to investigate the multi-scale variability of water dynamics in the southern GoT: from tidal to annual scales. The remainder of this paper is organized as follows: In Section 2, the location of the study area and physical forcing that controls the water dynamics are presented, and the data available, the configuration of the HFR system in Vietnam, and the analysis methods are described. We also evaluated the performance of the HFR data by comparing it with the in situ current measurements using an acoustic wave and current profiler (AWAC). The comparison is briefly described in the subsection of Section 2. In Section 3, the results are presented. Finally, the discussion and conclusions are provided in Sections 4 and 5, respectively.

2 Data and methods

2.1 Study area and environmental forcing

The GoT is a shallow, semi-enclosed, crescent-shaped marginal sea that lies between 17 and 22° N in the northern part of the SCS (Fig. 1). The gulf is 270 km wide and is bordered by the Vietnamese coast in the west, the Chinese coast in the north including the Leizhou Peninsula, and Hainan Island (China) in the east. The gulf is connected to the South China Sea mainly through the southern entrance, which is 230 km wide and 100-m deep. Another entrance is the shallow and narrow Hainan Strait (18 km wide and 50-m deep) in the east. The bottom topography of the gulf is rather complex. There are about 2000 small islets inside the gulf, which are mostly concentrated in the northwestern area. The northern part of the gulf is very shallow and characterized by a slight decrease in depth from 10 to 30 m. The southern part of the gulf is deeper (depth about 40 to 70 m). Large bathymetry gradients are observed along the Hainan Strait and in the southern part, especially along the coastline.

Tidal motions are generated in the GoT by progressive surface gravity waves coming from the open ocean. The tidal wave enters the gulf mainly through the southern entrance and progresses along the western coast of Hainan Island (Nguyen et al. 2014). Conversely, the Hainan Strait is a region with the strongest tidal energy dissipation, thus leaving little energy of tidal flux entering or escaping the gulf (Nguyen et al. 2014). The tidal regime in the northern gulf is predominantly diurnal. In the southern part of the gulf, the tidal regime is mixed diurnal. The amplitude of the dominant constituents K1 and O1 reaches 80 and 90 cm, respectively (Piton et al. 2020). At the southern entrance of the gulf, the diurnal components already dominate the semi-diurnal components. Here the diurnal tidal energy fluxes (K1 and O1) are three times larger than that of M2 tide and 20 times larger than that of S2 tide (Nguyen et al. 2014). Inside the gulf, the resonance of the diurnal tidal waves due to the basin topography and the degeneration of semi-diurnal components creates a unique diurnal tidal regime.

Located within the East Asian monsoon system, the circulation in the GoT is largely controlled by the Asian monsoon system, which is characterized by two distinct seasons: northeast (NE) monsoon and southwest (SW) monsoon (Wyrtki, 1961; Nguyen et al. 2014). The surface circulation in the GoT experiences a large seasonal variability and is strongly influenced by the two dominant climatic conditions. The NE monsoon (occurs in late fall to the end of winter, or dry season) lasts from October to February and is characterized by prevailing strong north and northeastern wind. The SW monsoon (in summer or wet season) lasts from May to August and is influenced by persistent southwestern wind. Tropical typhoon often occurs during this time. Between these climatic conditions, two transition periods are observed: early March to April, when the northeast wind gradually slows down and reverses to the southeastern wind, and September to the beginning of October, with a relaxation of southwesterly wind (Nguyen et al. 2014). The monthly variability of the wind is demonstrated in Fig. 3.

Buoyancy forcing is dominant in the western region of the gulf, which is related to the seasonal advection of the Red River discharge in the northern part of Vietnam (Rogowski et al. 2019). The Red River (Fig. 1), which originates from China, is fed by two major rivers in the north of Vietnam (Da and Lo) before flowing seaward. The average discharge rate of the Red River is 3500 $m^3 s^{-1}$ through nine distributaries along the 150-km coastline (Vinh et al. 2014). The peak discharge rate can exceed $1.0 \times 10^4 m^3 s^{-1}$ during some wet years (Chen et al. 2012; Ding et al. 2013). The discharged freshwater is confined to the Vietnamese coast and advected southward along the coast. In summer, under persistent southwesterly winds, the freshwater can move northward in a

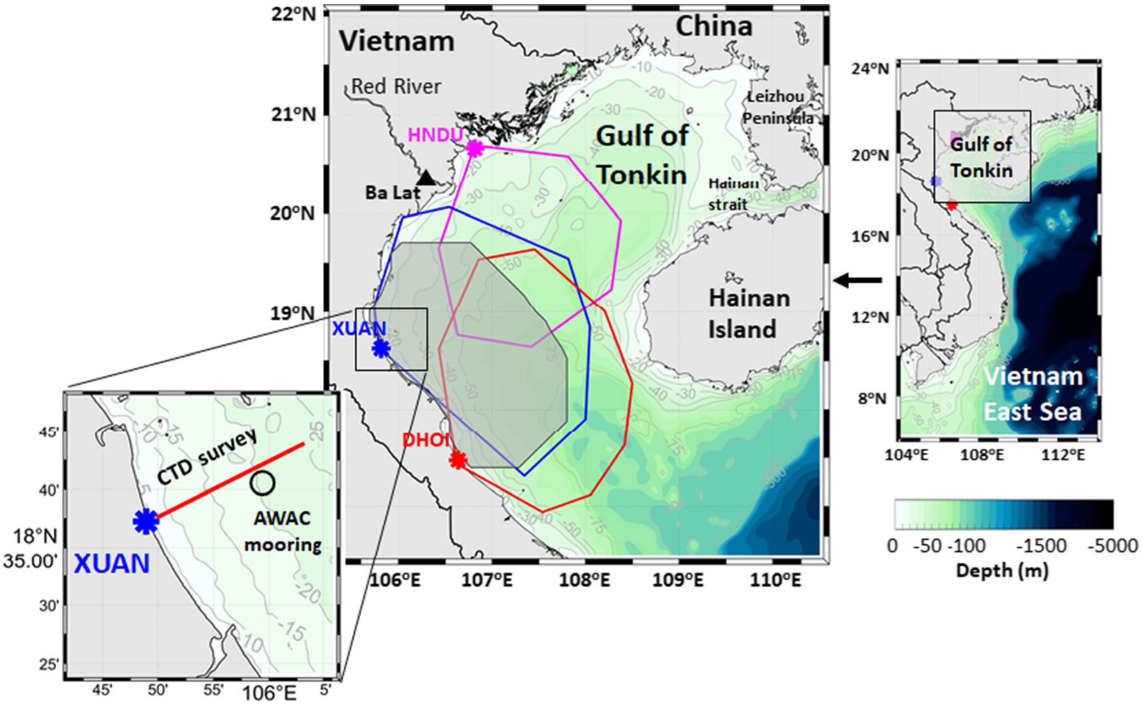

Fig. 1 Location of the Gulf of Tonkin and radar sites (color stars). Individual radar coverage is given in the color line. The study area where analysis of the radar-derived current velocities is performed is shown by gray shading. Also shown is the location of the AWAC mooring site (circle), monthly CTD transects (red line), and hydrological station at Ba Lat (triangle). The bathymetry is shown by color shading with bathymetry contours given by gray lines. Geographic names used in the text are also shown

counterclockwise motion and is described as "trapped" (Ding et al. 2013; Rogowski et al. 2019). Given the large contribution of freshwater discharge to the local dynamics, this GoT region is considered a complex region of freshwater influence (ROFI).

2.2 Data

2.2.1 HFR data

HFR system is land-based systems providing near synoptic observations of surface current for cost-effective operation complementary to traditional ship-based and moor-based stations, which are logistically challenging and expensive (Fujii et al. 2013). HFRs measure the ocean surface currents using the "Bragg scattering" principle. The resonant backscattering (Bragg scattering) results from the coherent reflection of the transmitted wave by the ocean waves which wavelength is half of that of the transmitted one. Although referred to as "radar," HFR systems operate at much longer wavelengths (normally ranging from 10 to 100 m). The electromagnetic wave transmitted from the radar is scattered off by ocean waves and is returned to its source. Through the Doppler spectrum analysis, radial velocities can be inferred in the direction toward or away from the radar. At least two radars are normally used to reconstruct a total vector from each site's radial components. The readers may refer to Paduan and Washburn (2013) for a thorough discussion on oceanographic HFR theory, development, and applications.

The HFR network in Vietnam is operated by the Center for Oceanography, Vietnam Administration of Sea and Islands (CFO, VASI). Individual sites are located at the Hon Dau Island (HNDU, 106.81° E, 20.67° N), Nghi Xuan (XUAN, 105.82° E, 18.62° N), and Dong Hoi (DHOI, 106.64° E, 17.47° N) (Fig. 1). The long-range HFRs are configured to operate at a frequency of 4.625 MHz (which was changed to 5.25 MHz in 2018). The radial velocity components are measured by the radar at an effective depth of 2.4 m. This effective depth is determined as $\lambda_R/8\pi$, where λ_R denotes the radio wavelength (Stewart and Joy 1974). The following configuration has been used at each radar site to retrieve the radial velocities of the surface currents: 5.8 km along the beam and azimuthal spacing 5°. The temporal resolution was set to 1 h.

In this study, hourly HFR radial velocities were obtained at XUAN and DHOI radar sites for more than 2 years (from April 2014 to October 2016) and mapped using EOF/variational interpolation methods (described in Section 2.3). The data from the HNDU site were neglected, because the site suffered from numerous hardware failures during this period. Figure 2 presents the temporal coverage of the XUAN and DHOI sites. Conversely, the spatial coverage was highly sensitive to the conditions of the sea state. The coverage was found to be larger during winter and spring (October to the end of April). During summer (May to September), the HFR

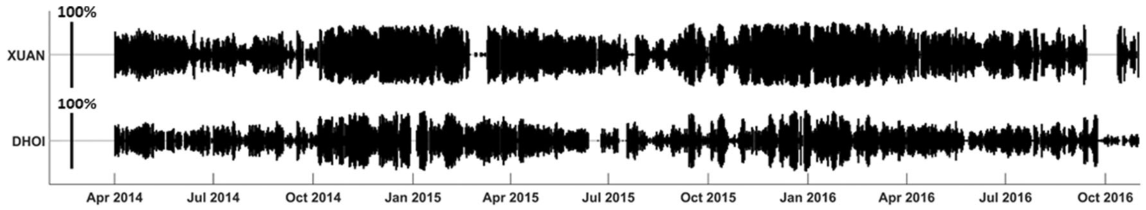

Fig. 2 Time history of the data return for two individual radars from April 2014 to October 2016. The height of each line matches the percentage of data availability. The scale bar on the left represents the maximum coverage (the maximum data return)

records exhibit a gradual drop in the coverage area of the obtained data. During summer, the wind direction reverses from northwest to southeast (onshore to offshore wind); thus, the ocean waves (Bragg waves with a wavelength of 30 m) do not gain sufficient fetch. During this period, a lower sea state results in lower coverage by coastal radars (Rogowski et al. 2019).

2.2.2 In situ velocity measurements

In 2015, a bottom-mounted current profiler AWAC, which operates at 600 kHz, was deployed offshore the XUAN radar site (105.97° E, 18.68° N) at a depth of 20 m and provided data for roughly 14 days (from October 16 to October 30, 2015). The instrument was configured to measure the current velocity profiles at 0.5-m vertical resolution and temporal resolution of 30 min.

2.2.3 Reanalyzed wind data

To evaluate the influence of wind on the surface currents, the wind data were obtained from the European Centre for Medium–Range Weather Forecasts (ECMWF) reanalysis model with a time step of 6 h and spatial resolution of 0.125° (https://www.ecmwf.int/en/forecasts/datasets/reanalysis-datasets/era-interim). The 3-year reanalyzed wind data (from 2014 to 2016) were used to demonstrate the variability of the winds by the wind rose plots in Fig. 3. Wind stress was calculated using the formula of Large and Pond (1981): $\overline{\tau} = \rho C_d |w| \overrightarrow{w}$ with $C_d = 1.15 \times 10^{-3}$. The wind speed and direction were then interpolated on the HFR grid.

2.2.4 Monthly CTD surveys and climatological river discharge

Monthly CTD surveys were conducted off the coast of the XUAN radar site during the period from September 2015 to August 2016. The transect extends 25-km offshore, with measurements spaced every 2.5 km (Fig. 1). Temperature and salinity profiles were obtained by boat-based, hand-deployed RBR Concerto CTD sampling at 16 Hz. The freshwater discharge data, available at the Ba Lat station, located 11-km inland from the river mouth, do not cover the whole period of observations. Thus, we used the climatological data to demonstrate the evolution of the river plume. These data were obtained in the framework of a collaboration project between the Vietnamese institutes (CFO, VASI) and the US institutes (Scripps Institution of Oceanography, Oregon State University, and Rutgers University).

2.3 Methods for data processing and analysis

2.3.1 HFR data processing and interpolation

After the quality control, the gaps in the radar data were filled in. The issue of filling the missing values in the HFR records has been explored over a long time. Several techniques have been investigated, such as the open-boundary mode analysis (OMA) by Kaplan and Lekien (2007), optimal interpolation

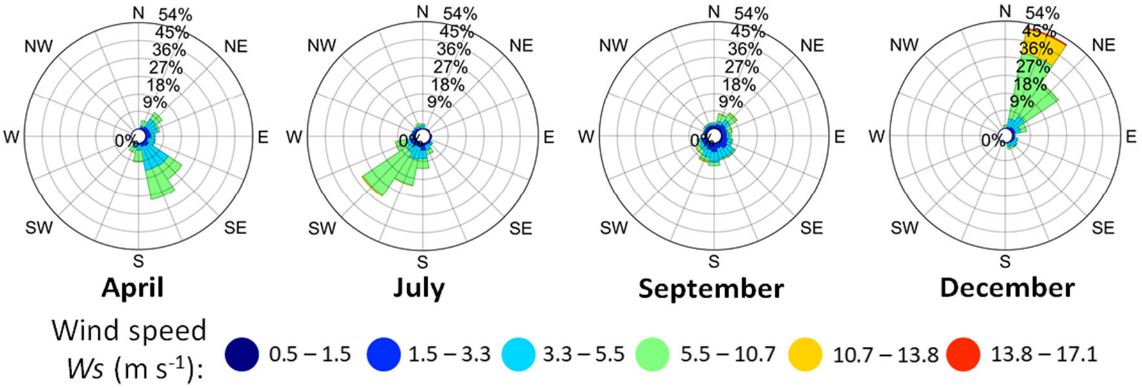

Fig. 3 Wind roses for four climatic conditions: NE monsoon (in December), SW monsoon (in July), and two transition periods: from NE to SW monsoon (in April) and from SW to NE monsoon (in September). The reanalyzed wind data were used from 2014 to 2016

(OI) by Kim et al. (2008), and EOF/variational interpolation (EOF/2dVar) by Yaremchuk and Sentchev (2011). The 2dVar method has several advantages compared to other techniques of radar data interpolation. 2dVar is a non-local and kinematically constrained interpolation method. It uses a combination of all measured velocities to reconstruct the velocity vector in one location and therefore, it creates a surface current velocity map. The 2dVar method is more flexible than OMA (also non-local interpolation method) in the choice of regularization. The smoothness of the interpolated vector field is enforced by penalizing the squared Laplacian of the velocity and also of its curl and divergence, thus providing the algorithm with adjustable and efficient control of smoothness. Kinematic constraints (zero flux on the rigid boundary), incorporated into 2dVar, appear particularly useful in regions with a complex shoreline and islands located inside of the interpolation area. Moreover, at the pre-processing step, the 2dVar method can use the iterative EOF-based technique for filling the gaps in the radial velocity time series. This makes the method particularly effective in case of radar failure or malfunctioning during short periods.

In our study, we used the EOF/2dVar method proposed by Yaremchuk and Sentchev (2011) to map the surface currents from the HFR measurements. The method is decomposed into four consecutive steps: (a) EOF analysis of the spike-removed radial velocities, (b) estimation of the inverse of velocity error covariance and signal-to-noise separation, (c) filling of gaps in radial maps, and (d) interpolation of the surface current velocities on a regular grid using a variational method (2dVar) and current vector map generation. Although both OMA and 2dVar are found to be capable of filling the gaps in space, the EOF/2dVar method is also capable of filling the gap in the HFR records, both at the spatial and temporal scales. The method had demonstrated the ability to fill the gaps up to 2 days, depending on the optimum number of EOF modes used in the decomposition of the time series. The detailed descriptions of the method are presented in the study by Yaremchuk and Sentchev (2011).

2.3.2 Principal component analysis, rotary spectral analysis, and tidal harmonic analysis

We conducted rotary spectral analysis (hereafter referred to as RSA) of the HFR data to retrieve prominent frequencies of surface current variability in the GoT. The method was used to process a 2.5-year-long HFR data and reanalyzed wind from April 2014 to October 2016. In addition, we analyzed a 3-month-long cumulative time series during summer (June to August) and winter (November to January) to evaluate the effect of seasonal variability of wind on currents.

The principal component analysis (PCA) technique was used for the HFR-derived velocities to access tidal motions. This technique enables us to estimate the contribution of all tidal constituents to the observed currents. PCA provides the parameters of synthesized tidal current ellipses: the orientation and magnitude of the dominant currents. The drawback of the PCA is that it does not provide information on the sign of current vector rotations. Therefore, the rotary coefficient was estimated from the RSA of the surface current velocities. The RSA exhibits pronounced peaks in the energy spectrum $S(f)$ at diurnal frequencies (K1 and O1) and semi-diurnal frequency (M2) corresponding to both clockwise (*cw*) motion S_- and counterclockwise (*ccw*) motion S_+ of the current vector rotations. The rotary coefficient, which is defined as $r = (S_+ - S_-)/(S_+ + S_-)$, was estimated at every grid point from these peak values. The value of r ranges from − 1, for *cw* rotation, to 1, for *ccw* rotation.

The harmonic analysis was applied to the 1-year-long time series of surface current using the T_tide package (Pawlowicz et al. 2002). Nodal corrections were included in the analysis of tidal currents.

2.3.3 Seasonal variability of coastal water stratification

To evaluate the seasonal variability of stratification in the coastal zone generated by the freshwater discharge variations in the Red River, we used the potential energy anomaly (PEA) index ϕ proposed by Simpson et al. (1990):

$$\Phi = \frac{1}{h}\int_{-h}^{\eta} gz\left(\overline{\rho}-\rho\right)dz$$

Here, h denotes the water depth in meters; η is the sea surface height with respect to depth; ρ is the potential density at depth z; $\overline{\rho}$ is the vertically average potential density; and g is the gravitational acceleration. The value of Φ indicates the amount of required energy per unit volume to completely mix the water column. Thus, it represents the strength of the water column stratification. Zero value means the column is fully mixed and it increases with stratification. In this study, we consider that values smaller than 5 J m^{-3} represent mixed conditions, while values greater than 10 J m^{-3} corresponds to highly stratified conditions, and the values in between correspond to weakly stratified conditions. The intermediate values, between 5 and 10 J m^{-3}, correspond to weakly stratified conditions. The CTD profiles were obtained along the transection off the coast of the XUAN radar site and limit to the upper layer 26 m thick. Therefore, the analysis of the time evolution of water stratification in this study is limited to the subsurface layer.

2.4 Validation of the HFR data and assessment of the data interpolation techniques

To assess the overall performance of the HFR observations, we compared the HFR-derived current velocities with in situ current measurements by AWAC, following the method proposed by Liu et al. (2014). The first complete bin of AWAC-derived current velocities below the surface at a depth of 2 m was compared with that derived from HFR. The skill metrics include bias, root mean square error (RMSE), and complex correlation analysis between HFR-derived velocity and AWAC velocity time series (Kundu 1976). We investigated both the differences between the AWAC current meters and the HFR total current processed using the OMA solution and the EOF/2dVar method. Three sets of radar-derived velocity were compared with the AWAC data: (1) the radial velocities reprocessed by the OMA method; (2) the velocities after the gap filling by EOF and reprocessed by the OMA method; and (3) the velocities reprocessed by the EOF/2dVar with gap-filling capability. The results, which are presented in Table 1, reveal that all methods provide a good complex correlation between the AWAC and radar velocities. The absolute correlation values (α) are larger than 0.7. The phase difference (θ) for each of the three cases is less than 3° and demonstrates a rotation of the HFR-derived current vector to the right of the AWAC-derived current vector. Quantitatively, the bias between the AWAC and HFR is about 0.03 m s^{-1} for the zonal components for the three cases and less than 0.06 m s^{-1} for the meridional component. In terms of RMSE, the differences are found to be less than 0.14 m s^{-1} for both components. Generally, the radar-derived velocities processed by EOF/2dVar exhibited a slightly better agreement with the AWAC measurements than those processed by the OMA method (Table 1).

3 Results

3.1 Spectral analyses of wind speed and current velocity

Figure 4 presents the rotary power spectral density (PSD) of the wind speed while Fig. 6 presents the PSD of the surface current velocities. The PSD of the wind speed shows the energy cascading from large to small scales (the spectral slope is a − 5/3). It also shows well-defined peaks at the diurnal, semi-diurnal, and third-diurnal peaks. The wind spectrum in winter exhibits notable peaks in the sub-diurnal band (0.0205 and 0.0085 cph), which are related to the strong northeasterly wind often varying the intensity with a period of 2–5 days (Fig. 4b). The prominent diurnal peak in Fig. 4c could be due to the so-called sea breeze, which is supported by higher energy level in wind variability at diurnal frequency in summer. The energy at the diurnal frequency of the wind is larger by an order of magnitude than that at semi-diurnal frequencies, especially in summer. This is due to the large differences in the land-sea temperatures at this period. For example, on June 11, 2019, the temperature observed from Ha Tinh and Dong Hoi provinces, which are the locations of the XUAN and DHOI radar sites, respectively, exceeded 43 °C. The difference in the land-sea temperature in these areas could reach 15 °C (data retrieved from Vietnam National Center of Hydrological and Meteorological Forecast: *www.nchmf.gov.vn*).

Three prominent peaks at diurnal (O1, K1) and semi-diurnal (M2) frequencies are identified in the current velocity spectrum (Fig. 5a). The energy of the diurnal tidal constituents is higher than that of the semi-diurnal constituents by an order of magnitude (1.5 10^{-2} and 1.6 10^{-3} m^2 s^{-2} cph^{-1} respectively), indicating that diurnal tide dominates the tidal dynamics in the GoT. Smaller peaks in Fig. 5 correspond to the third-diurnal shallow-water tidal constituents (SK3, MK3, MO3) (Pawlowicz et al. 2002). These higher order tidal harmonics are generated by nonlinear interactions of the main diurnal and the semi-diurnal tidal constituents in the shallow waters. However, the magnitude of these nonlinear tidal harmonics is extremely low (less than 0.02 m s^{-1}) compared to that of four main tidal constituents.

Both the ccw and cw motions have similar energy level at the diurnal frequency (the peaks at K1 and O1 in Fig. 5a). This suggests that, for these two harmonics, the tidal current is reversive, i.d. the current vector variation is rectilinear. However, the energy of the cw motion at the semi-diurnal frequency (M2) is higher by half an order of magnitude than that of the ccw motion, thus resulting in a more circular shape of the tidal current ellipses.

The influence of the wind on the surface current is also visible at the inertial frequency of 0.026 cph (period of 38 h). The cw motion is greater than the ccw component by half an order of magnitude (Fig. 4).

Considering the seasonal change in the surface current kinetic energy spectrum, there are notable power density variations at different frequencies (Fig. 5b, c). In winter, the energy at the diurnal frequency is higher in winter than in summer by about roughly a half of an order of magnitude (1.5 10^{-2} and 6 10^{-3} m^2 s^{-2} cph^{-1} respectively) (Fig. 5b, c), whereas opposite

Table 1 Results of comparison of HFR velocities processed by three different methods and in situ velocity measurements at AWAC mooring. The period of measurements spans from October 17 to October 29, 2015

Method	Correlation		BIAS (m s^{-1})		RMSE (m s^{-1})		α	θ
	U	V	U	V	U	V		
HFR OMA vs AWAC	0.66	0.82	−0.04	0.06	0.14	0.12	0.74	−2.57°
HFR OMA + Gap filling vs AWAC	0.70	0.84	−0.03	0.04	0.14	0.10	0.75	−1.06°
HFR 2dVar + gap filling vs AWAC	0.78	0.85	−0.03	0.03	0.12	0.10	0.79	−0.93°

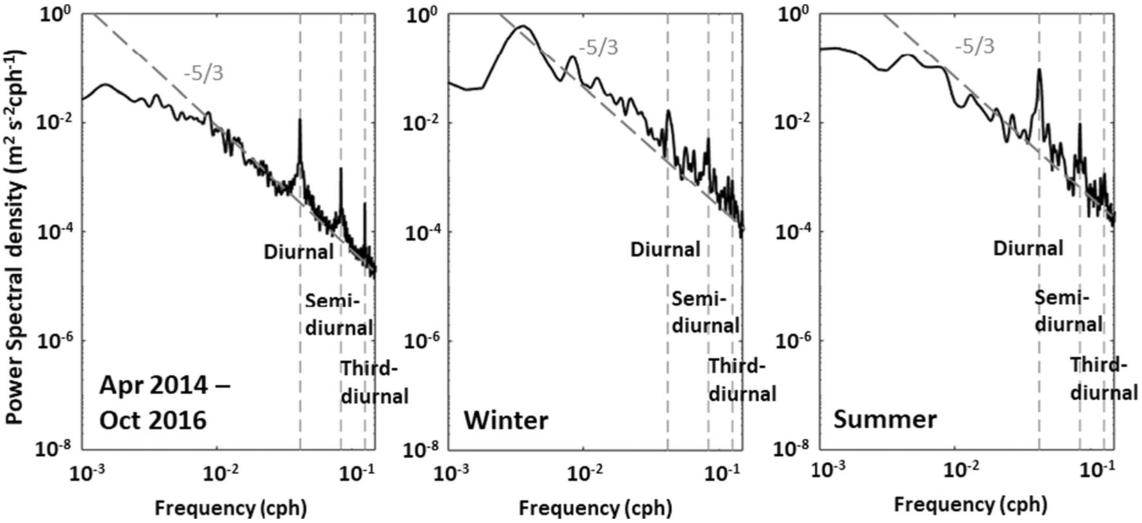

Fig. 4 Basin-wide average power spectral density for reanalyzed wind speed for the whole 2.5-year-long period of analysis from April 2014 to October 2016 (**a**), for the winter period (November 2014 to January 2015) (**b**), and summer period (June to August 2015) (**c**)

distribution is observed in the wind spectra where the peak at the diurnal frequency in summer is higher than in winter by half an order of magnitude ($5\ 10^{-2}$ and $1\ 10^{-2}\ m^2\ s^{-2}\ cph^{-1}$ respectively) (Fig. 4b, c). Contrarily, the inertial peak in the PSD of the currents in winter becomes less significant and shifts toward the subinertial band (less than 0.026 cph). The variability of the current velocities with a period of 2–5 days (Fig. 5b) is similar to that of the wind also observed in winter (Fig. 4b).

3.2 Tidal currents

3.2.1 Space-time variation of the tidal currents

The PCA method was used to analyze hourly velocities recorded by HFR for 17 days, from October 13, 2015, to October 31, 2015. This period corresponds to the period of AWAC measurements (Fig. 6). The evolution of tidal currents in both the space and time domain is quantified using the synthesized ellipses derived from the PCA and rotary spectral analysis.

The tidal wave propagating southward is controlled by the topography and is characterized by the lower eccentricity of tidal ellipses (flatter tidal ellipses) oriented parallel to the shoreline. The magnitude of the tidal currents, as presented by the length of current ellipses, is high at the southern entrance, with values ranging from 0.4 to 0.6 m s^{-1}, then decreases (0.05 to 0.2 m s^{-1}) in the northern part. A major branch of tidal energy enters the gulf through the southern entrance, and a large part of incoming tidal flux tends to be deflected to the right along the Hainan Island (Nguyen et al. 2014). Subsequently, the tidal magnitude near the gulf entrance is slightly higher in the offshore zone (0.5 to 0.6 m s^{-1},

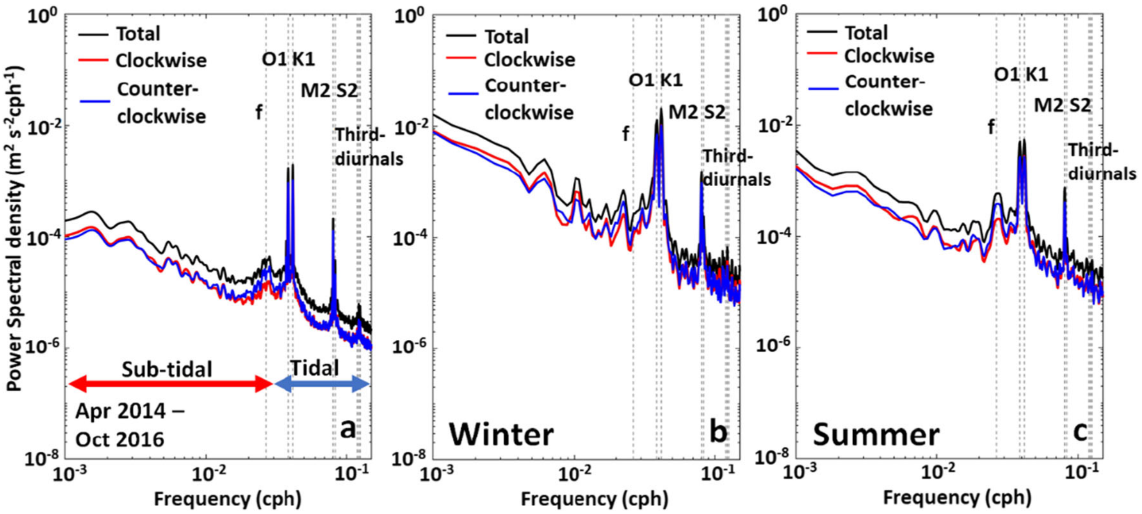

Fig. 5 Basin-wide average power spectral density for surface current velocities for the whole 2.5-year-long period from April 2014 to October 2016 (**a**), in winter (November 2014 to January 2015) (**b**), and in summer (June to August 2015) (**c**)

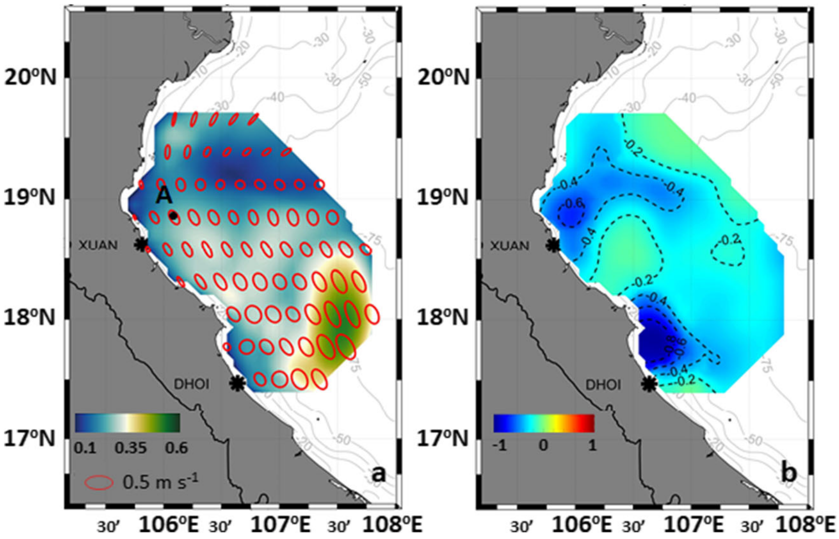

Fig. 6 **a** PCA-derived tidal ellipses during a 17-day period from October 13, 2015, to Oct 31, 2015. Tidal ellipses are plotted every tenth grid points. Red ellipses denote the clockwise rotating current vectors. The major axis of the ellipses indicates the tidal magnitude in m s^{-1} (color shading). **b** Rotary coefficient of surface current velocities during the same period (color shading and contour lines). Black point A corresponds to the AWAC mooring location

Fig. 6a). The energy of the tidal wave traveling in the gulf dissipates due to the effect of bottom friction, and the resulting amplitude of tidal currents gradually decreases with decreasing depth in the northern sector (Fig. 6a).

The spatial distribution of the rotary coefficient (Fig. 6b) exhibits a complex pattern. The tidal current vectors in the GoT are dominated by the cw rotation, with the average value of rotary coefficient ranging from − 0.1 to − 0.3 in the middle part of the gulf. Lower values (from − 0.6 to − 0.4) are observed in the shallow water area along the Vietnamese coast and in the region located between the two radar sites.

PCA was also applied to evaluate the temporal variability of the tidal currents at the location of the AWAC mooring (point A in Fig. 6a) during a whole tidal cycle from October 13, 2015, to November 08, 2015. During this period, a fortnightly variation of tidal current occurs, and both the primary and secondary spring tides are observed in the time series of the tidal ellipse evolution (Fig. 7). The tidal amplitude increases from 0.07 m s^{-1}, on October 13, to 0.36 m s^{-1}, on October 20. The comparison suggests that both the HFR-derived and AWAC-derived ellipses exhibit similar magnitudes and shapes. The mean bias in the magnitude of the AWAC- and HFR-derived tidal current is 3 cm s^{-1}. In spite of a good overall agreement, a larger discrepancy of about 10 cm s^{-1} between HFR- and AWAC-derived tidal ellipse magnitude is observed on October 26, 2015. On this day, the radar measurements showed a stronger southward current than that observed AWAC (Fig. 15). The difference can arise from the scale of motions resolved by two measurement techniques: point measurements by AWAC and spatial averaged velocity obtained by HFR. It can also result from technical problems of data acquisition by HFR on this particular day.

3.2.2 Tidal harmonic analysis

Figure 8 presents the results of the harmonic analysis of the tidal current velocities. The spatial distribution of the total velocity variance indicates that tidal motions account for a large percentage of surface current variability in the GoT. This contribution ranges from 20% in the shallow water zone near the Red River mouth and in the middle of the domain to 70% at the southern entrance of the gulf. The mean tidal contribution to the total surface variability is 60%, which is obtained by averaging the percentages over the study region. Typically, the variability of the velocity is much larger in the north-south direction (V-component) than in the east-west direction (U-component) as the tides enter the gulf mainly through the southern open boundary.

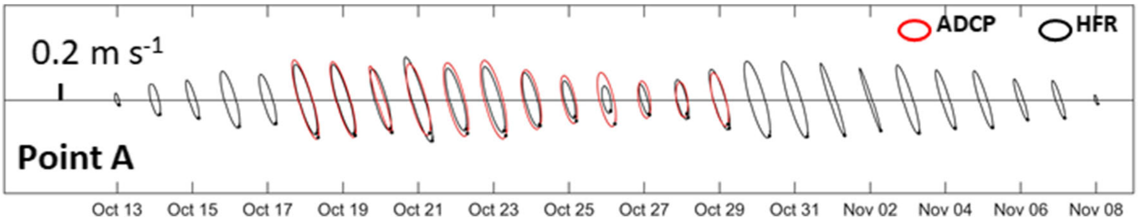

Fig. 7 Time evolution of tidal current ellipses at point A (at the AWAC mooring location) from October 13, 2015, to November 08, 2015. HFR-derived current ellipses are shown in black and ellipses from ADCP measurements are shown in red. The major axis of ellipses denotes the tidal current magnitude. The scale of the tidal ellipses is shown on the left side

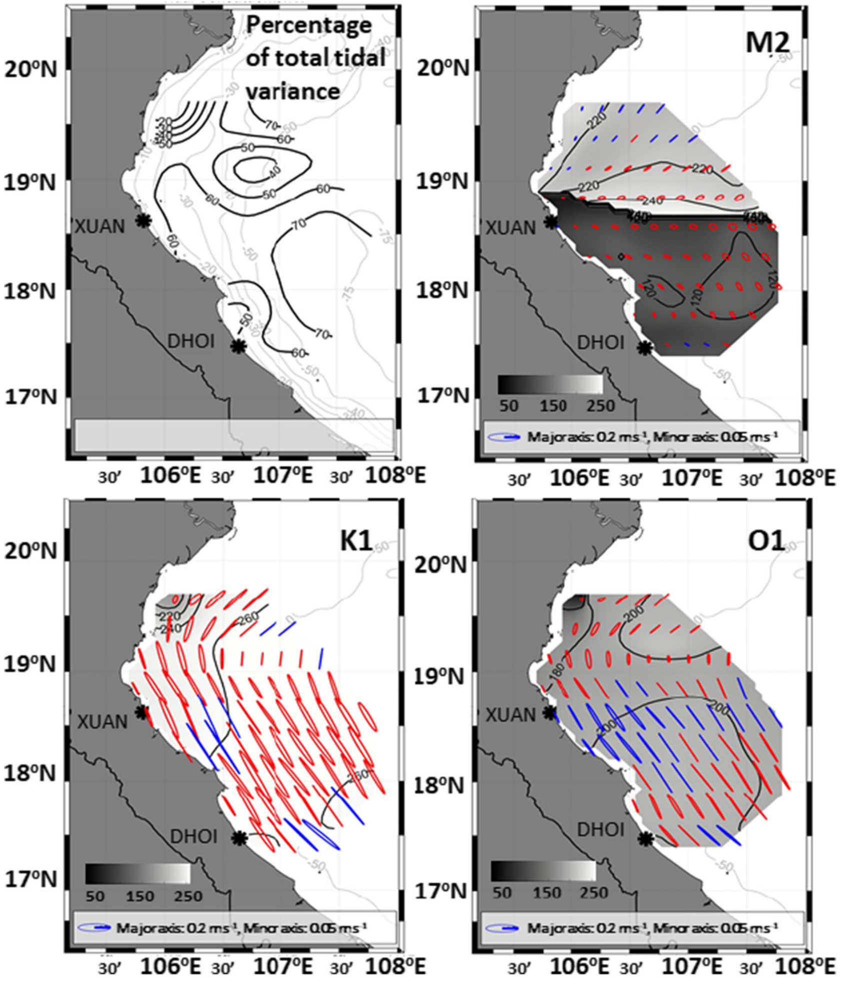

Fig. 8 Contribution of tidal motions to the total variance of surface current velocities (left top panel). Tidal current ellipses and corresponding phase distribution (gray shading and contour lines) for three dominant tidal constituents (O1, K1, and M2) were derived from the tidal harmonic analysis. The current vector rotation is shown in blue for ccw and in red for cw rotating currents

The spatial patterns of the tidal ellipses of the predominant diurnal constituents (K1 and O1) are quite similar in terms of structure. The cw motion of the K1 constituent dominates most of the domain, whereas the ccw motions of the O1 constituent are concentrated in the middle of the domain. The tidal ellipses are tightened and strongly controlled by the basin configuration. The tidal magnitude ranges from 0.05 m s^{-1}, near the river mouth and in the middle of the gulf, to 0.2 m s^{-1}, at the southern limit of the gulf. A comparison of the phase distribution for the tidal elevation and the tidal currents indicates a combination of standing wave and progressive wave motions. The phase of surface elevation for predominant diurnal tidal constituents ranges from 100° to 120° for the K1 constituent and from 30° to 40° for the O1 constituent (Nguyen et al. 2014; Piton et al. 2020), whereas the phases of tidal currents are about 260° for the K1 constituent and 200° for the O1 constituent on average. The footprint of a standing wave in the northeast-southwest direction can be inferred from the difference in the phase of tidal current and elevation (close to quadrature) near the coast in the northern part of the gulf. Thus, the tidal dynamics in the northern gulf is similar to that of the standing wave (Nguyen et al. 2014).

The amplitude and phase distribution of the semi-diurnal tidal current constituents are quite complex. The magnitude of the M2 constituent, which ranges from 0.02 to 0.05 m s^{-1}, is lower than the diurnal tides by a factor of 4. The phase distribution of the M2 constituent rapidly changes from 220° in the northern sector to 120° in the southern sector (Fig. 8b). The spatial distribution of phase lags and tidal ellipses orientation suggest that a tidal wave has the form of a progressive Kelvin wave and travels in the southwest direction along the coast of Vietnam. The shape of the tidal ellipses and phase distribution of S2 (not shown) tidal ellipses and phases are almost identical to those of M2. However, the magnitude of S2 harmonic, which ranges from 0.01 to 0.02 m s^{-1}, is lower than that of the diurnal tidal harmonics by a factor of 8. A combination of the major tidal constituents gives the total tidal ellipse a more circular shape in the southern part of the domain (Fig. 6a).

3.3 Sub-tidal variability of the surface currents

The sub-tidal variability of the surface currents was evaluated after applying to HFR-derived velocities a low-pass filter with a 38-h cutoff. The pl66tn (Beardsley and Rosenfeld 1981) low-pass filter was used to create hourly filtered data. The same filter was also applied to wind data.

3.3.1 Annual mean surface flow and seasonal variability

The mean velocity distributions derived from the HFR measurements indicate a prominent southward flow along the coast of Vietnam (Fig. 9). The flow originates from the northern part of the gulf, follows the 30-m isobath, and experiences intensification between 18° N and 19° N. In the southern part, a separation of the coastal current into two branches is observed: one branch keeps flowing southward and the other changes the direction to offshore and then merges with the northward flow from the SCS. The annual mean circulation pattern is thus cyclonic.

The time series of the hourly current speed in 2015 were extracted at two points, one near the shoreline and another in the offshore region (point A and point B in Fig. 9), to assess the annual variability compared with the wind stress variability. In winter, the current magnitudes are stronger than in other seasons (at an average of 0.3 to 0.5 m s^{-1}), which is influenced by periodic strong northeasterly winds. Near the shore, the current speeds occasionally reach 0.8 to 1.0 m s^{-1} during strong wind (Fig. 10, middle panel) and can exceed the offshore current speed (the highest speed is about 0.6 m s^{-1}). A large difference in the nearshore and offshore current magnitudes, which could exceed 0.4 m s^{-1}, is observed from late September to early March, whereas from May to August, the difference is less significant (Fig. 10).

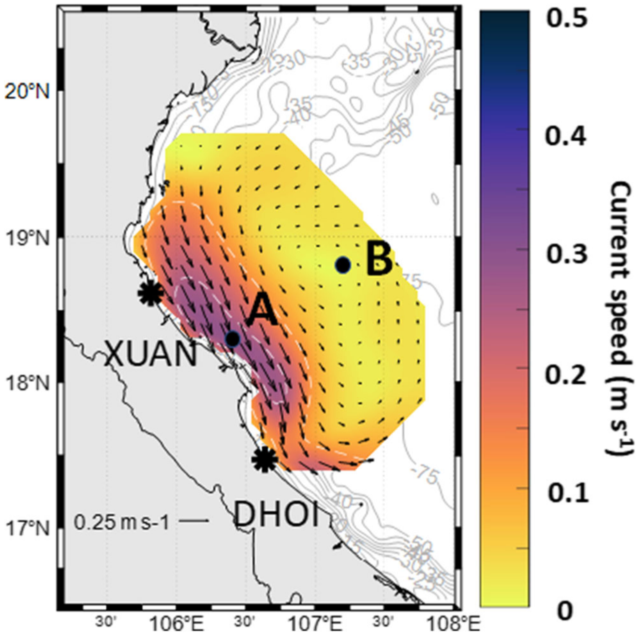

Fig. 9 Mean surface current velocity field during the period from April 2014 to October 2016. Surface velocities are plotted every 15 km. Points A and B correspond to the nearshore and offshore location selected for further assessment

Figure 11 a and b present the mean surface current fields for July (summer) and December (winter). The current velocity variance is estimated and presented as ellipses. From winter to summer with the wind direction reversal, the current speed gradually decreases from 0.4 to 0.2 m s^{-1}. Near the shoreline, the current speeds are stronger (0.3–0.5 m s^{-1}) than in the middle of the gulf (0.1–0.3 m s^{-1}). The mean values and variability presented in Fig. 11b suggest that the currents in winter are stronger and experience less variation than during other periods.

A Hovmoller diagram was used to better understand the seasonal evolution of surface circulation in the GoT (Fig. 11c, d). Monthly surface current data were extracted along the line perpendicular to the shoreline. The velocity vectors were projected onto two directions, normal and parallel to the cross section, thus providing two velocity components: along-shore and cross-shore. Negative along-shore velocities match the current directed southwestward. Positive cross-shore velocities match the offshore flow. The cross-section spans from the shoreline to approximately 150-km offshore. The same goes for the wind stresses extracted along the cross section (Fig. 11e).

As can be seen from the diagram, an annual cycle is observed for both the cross-shore and along-shore velocity components, which correspond to the wind forcing reversal. In the offshore zone, the velocity component normal to the cross-section line is quite low, with the value ranging from -0.1 to less than 0.1 m s^{-1}. In winter, the prevailing direction of the current is southward (Fig. 11c). Starting from April to the end of summer, the direction of the currents changes under the influence of prevailing southwesterly wind. A much stronger variability is observed in the nearshore zone. The along-shore current persists throughout the whole year, with a large amplitude of seasonal variability (from -0.25 m s^{-1} during winter to close to 0 during summer). The offshore extension of the area with a velocity larger than 0.1 m s^{-1} varies widely: 25–75 km. During the dry season (from September to February), a strong coastal jet with a velocity of more than 0.25 m s^{-1} is observed at a large distance from the shore (Fig. 11c).

From May to August, the velocity decreases to 0.1 m s^{-1}, and the spatial extension of the jet does not exceed 25 km from the shore. What is more surprising is the duration of the weak-strong stages of the coastal jet. Compared with the variations of the cross-shore velocity component (Fig. 11d), which is strictly periodic and associated with the wind variation, the modulation of the along-shore component appears different. The stage of a strong coastal jet lasts 8 to 9 months, whereas the stage of a weak jet lasts only 3 months (from June to August). Contrarily, the seasonal variability of the cross-shore velocity component follows the low-frequency variations of the wind.

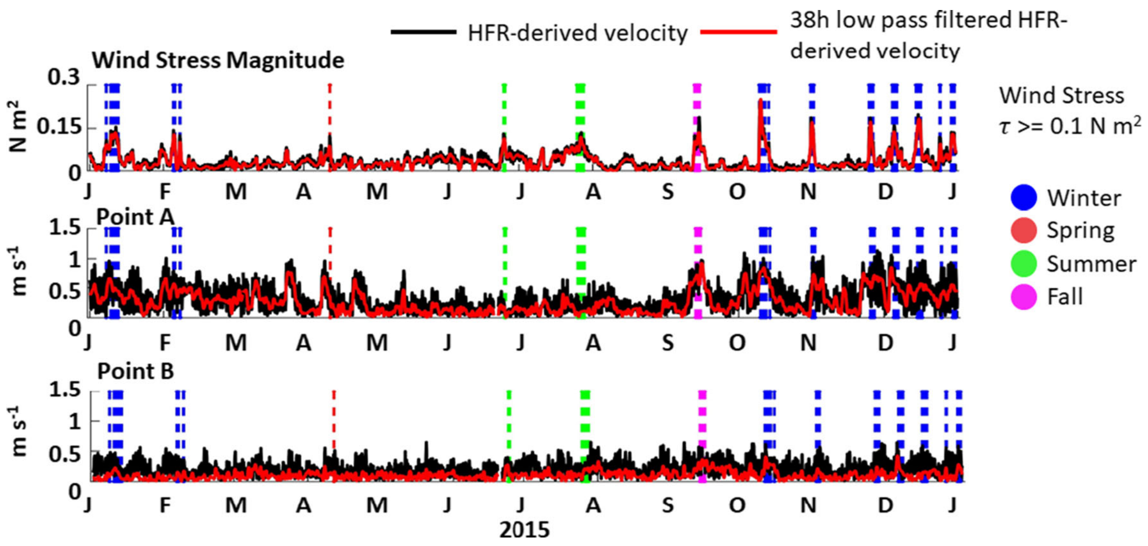

Fig. 10 Time series of spatial mean wind stress magnitude (top), the hourly current velocities (black line), and 38-h low-pass filtered velocities (red line) from the nearshore area at point A (middle), and from the offshore area at point B (bottom) in 2015. The color vertical lines mark the events of strong wind (wind stress magnitude greater than 0.1 N m^2)

3.3.2 Wind/current coherence analysis

To evaluate in detail the wind-current interactions and their spatial variability, we conducted a joint analysis of the wind stress and the observed current field. The obtained current velocities and wind stresses were projected on the cross-shore and along-shore directions (given by line A orientation in Fig. 11). Spatially averaged current velocities and wind stresses were considered after the spatial averaging of both the current and wind stress components at all data points and for each single time step. The analysis was performed, taking into consideration the 95% confidence level.

The first order of wind-current relationship is quantified by the lagged vector correlation (Kundu 1976) for the total time series and shows a significant correlation between the HFR-derived current and wind data (Fig. 12), with an absolute complex correlation value of 0.69 (Table 2). The spatial distribution of the correlation values shows an area of high values (0.5–0.6) in the northeast part of the domain, and an area of a lower correlation (0.3–0.4) near the shoreline. The distribution

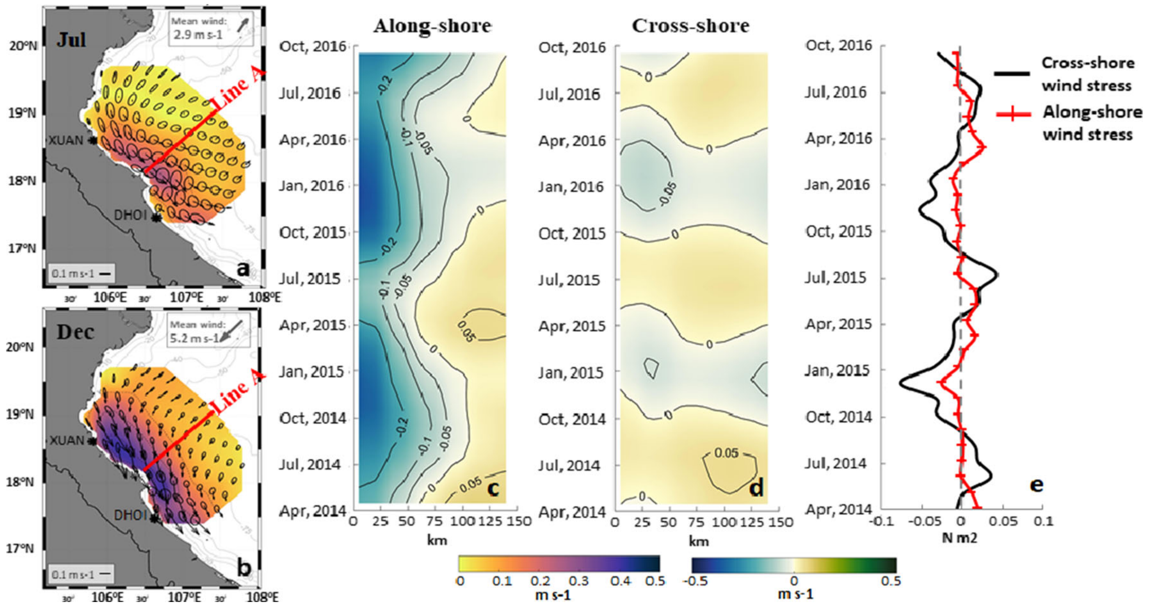

Fig. 11 Mean surface current magnitude (color shading) in summer (**a**) and in winter (**b**). Ellipses in **a** and **b** show the variance of the low-pass filtered current velocities. Space-time evolution of the along-shore and cross-shore surface current velocities along the transect A is shown in **c** and **d** by color shading. Monthly mean along and cross-shore components of the wind stress (**e**). Negative velocities indicate the southeastward and onshore current directions for the along-shore and cross-shore components respectively

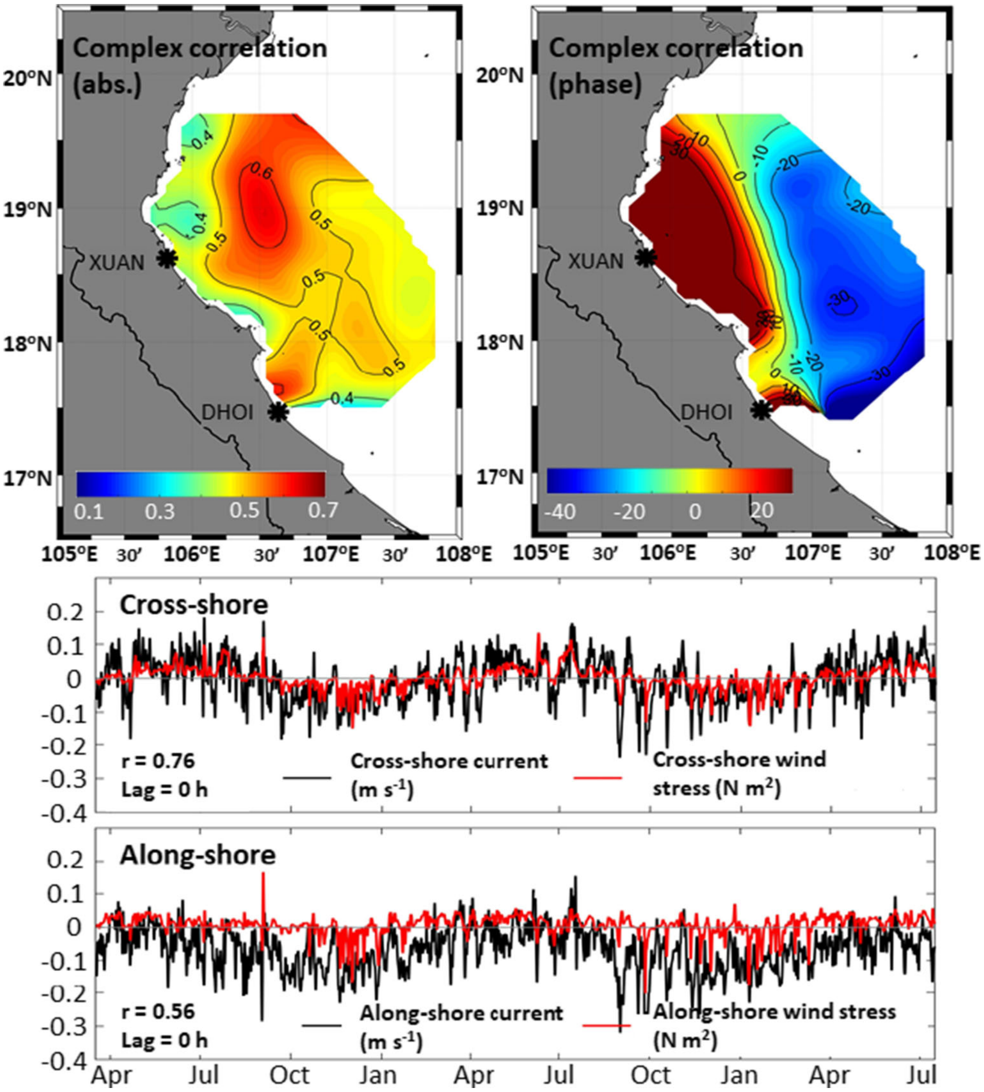

Fig. 12 Complex correlation between sub-tidal current velocities and wind stress. Contours are absolute values (left) and veering angles in degrees (right), negative values of veering angles mean that the current rotates clockwise from the wind. Time series of sub-tidal current velocity and wind stress components, from April 2014 to July 2016, are shown at two bottom sub-plots

of the phase correlation is complex, with negative values (− 30° to − 10°) overwhelming in the offshore area, whereas the positive values (10° to 35°) are found near the shoreline. The negative values in the offshore region reflect the tendency of the current to rotate clockwise with respect to the wind, which agrees with the Ekman theory. Positive veering angles near the shoreline are clearly related to the coastal currents previously mentioned. In addition, the time series of the domain-wide average exhibits a high correlation (0.76) between the wind stress and surface current for the cross-shore components, whereas, for the along-shore components, the correlation is significantly less (0.56). The seasonal cycle of the

Table 2 Correlations between the wind and surface current velocity components for different seasons and stratification conditions

		Cross-shore current vs. cross-shore wind	Along-shore current vs. along-shore wind	Complex correlation value	Complex correlation phase
Total		0.76 (lag=0 h)	0.56 (lag=0 h)	0.69 (lag=0 h)	−0.7° (lag=0 h)
Northeasterly wind	November 2014–January 2015	0.84 (lag=0 h)	0.68 (lag=0 h)	0.77 (lag=0 h)	5.7° (lag=0 h)
(well-mixed condition)	November 2015–January 2016	0.76 (lag=0 h)	0.50 (lag=0 h)	0.67 (lag=0 h)	3.2° (lag=0 h)
Southwesterly wind	June 2015–August 2015	0.55 (lag=6 h)	0.39 (lag=6 h)	0.48 (lag=6 h)	−35° (lag=6 h)
(weak stratified condition)	June 2016–August 2016	0.45 (lag=6 h)	0.50 (lag=6 h)	0.42 (lag=6 h)	−27° (lag=6 h)
Southwesterly wind	June 2015–July 2015	0.70 (lag=6 h)	0.53 (lag=6 h)	0.61 (lag=6 h)	−27.3° (lag=6 h)
(temporary mixed condition)	June 2016–July 2016	0.61 (lag=6 h)	0.32 (lag=6 h)	0.47 (lag=6 h)	−33.1° (lag=6 h)

current due to the wind reversal can be clearly observed in the cross-shore time series (mostly positive through April to August and vice versa). In addition, minimal lag at 0 h of both the time series indicates the nearly immediate response of the surface layer to the wind.

While the high correlation of the wind and surface current was obtained on average, there were some differences in the seasonal responses. To further evaluate the seasonal differences in wind-surface current responses, we extracted the data in the middle of two distinct periods: during the northeasterly (winter) and southwesterly wind (summer) conditions. After the seasonal separation, the high correlations (0.67 to 0.77) and small phase differences between wind and current vectors (5.7° and 3.2°) are observed between the surface current and wind data during winter (Table 2). The correlation between the cross-shore wind and current velocities is high (0.84) at the lag of 0 h, whereas a slightly lower correlation is observed for the along-shore components (0.68- at 0-h lag). High correlation and small phase differences indicate that the surface currents rapidly respond to the strong wind in winter. Under the strong wind, the surface currents are pushed onshore and travel southward along the coastline. The wind-induced current, thus, significantly contributes to the sub-tidal current variability during winter.

The correlation between the wind and current in summer is presented in Table 2. The surface current shifts toward the offshore direction following the change in the wind direction. The phase difference of − 35° indicates that the current vectors veer to the right of the wind direction. This is in agreement with the Ekman transport theory. In summer, the southwesterly wind is weaker than the northeasterly wind. The complex correlation is found to be significantly low (the highest is 0.48). Both along-shore and cross-shore components (the highest correlations are 0.55 and 0.50 respectively) exhibit a larger response time of 6 h. In addition, we analyzed the weakly stratified condition in mid-summer (approximately from mid-June to mid-July). After the freshwater was "trapped," the surface current somehow appears to be in phase with the variation of the wind as shown by the slight increases in the wind-current correlation (the highest complex correlation is 0.61 compares to 0.48 in this season) and the cross-shore components (0.70 compares to 0.55 respectively). From August toward the end of summer, the freshwater is released again thus inducing stratification and results in a decrease in the wind-current correlation.

3.4 Influence of freshwater discharge on surface currents

3.4.1 River plume variability

During the year, a large amount of riverine freshwater is discharged from July to September and the lowest is in mid-winter. The typical discharge in the Ba Lat station is at a rate of 1200 m^3 s^{-1}. The highest discharge in August is at a rate of 1400 m^3 s^{-1} whereas in January, the average discharge is low, typically around 500 m^3 s^{-1} (Fig. 13e). The monthly CTD transect survey data from the cross-shore transects (red line in Fig. 1) were analyzed to study the evolution of the Red River plume. While the monthly temperature transects allow the characterization of the seasonal cycle of the surface heat flux into the water column (results not shown), the salinity distribution helps understand the variability of the Red River coastal plume (Fig. 13a–d). Using the same data, Rogowski et al. (2019) demonstrated the seasonal variability of the Red River plume in the coastal zone. The freshwater plume, which is confined to the surface layer (about 5-m thick) and advected southward along the Vietnam coast at the end of summer, extends deeper into the water column from October onward (the observed fresher water is about 10-m deep and spreads outward to the sea beyond the survey line), thus inducing stratification (Fig. 13a). In winter, the decrease in the riverine discharge and the cooling of the seawater favors the mixing of the coastal water. The water column becomes well mixed in the middle of January (Fig. 13b), which coincides with the minimal discharge from the Red River. In April, the thin layer of freshwater observed on the surface suggests that the river plume continued to evolve (Fig. 13c). In mid-summer (late June), the transect data shows that the water became saltier, indicating that the river plume was trapped at the mouth of the Red River under southwesterly wind conditions and the denser water from the open ocean intruded into the shallow water zone (Fig. 13d).

Figure 13e presents the monthly variation of the PEA index ϕ which is calculated from the CTD transect survey data. From September to October, as the river plume is developed and advected southward, the water column is found to be highly stratified (the value of ϕ is 13 to 18 J m^{-3}). In winter, a decrease in the river discharge causes a decrease in ϕ, which matches the well-mixed conditions generally observed in December and January (the value of ϕ is 2 to 4.5 J m^{-3}). The second cycle of stratification increase starts in March and lasts until May. It is related to the southward advection of the freshwater coming from the river mouth. Mid-summer, which spans from June to July, is considered as the second mixed period. During these months, the coastal currents reverse, and the river plume is transported eastward. The decrease in the freshwater discharge influence on the southern coast of Vietnam creates favorable conditions for water mixing. This is supported by a local minimum of ϕ in June (the value of ϕ is 5.7 J m^{-3}).

3.4.2 River discharge and tidal straining

The PSD of the current velocities indicates that the power density at the diurnal and semi-diurnal frequencies changes

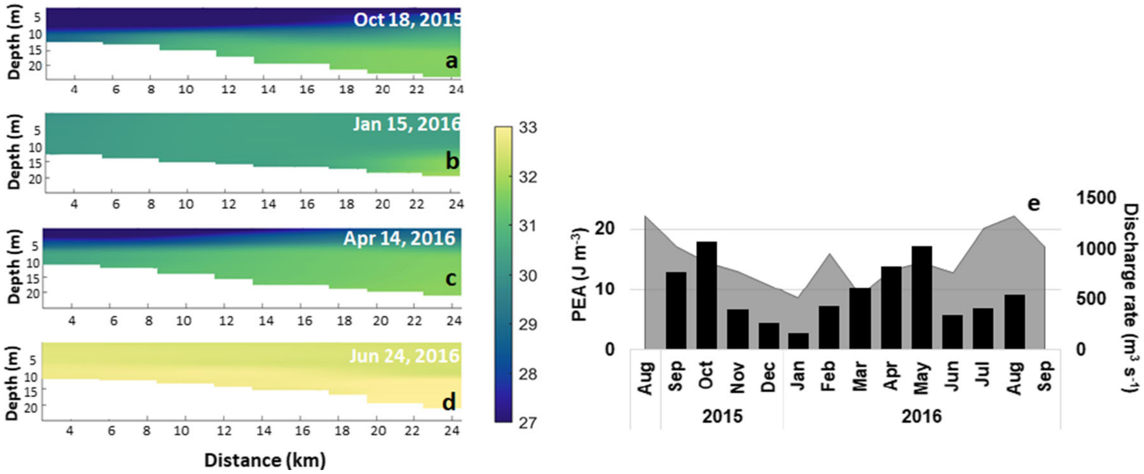

Fig. 13 Salinity variations along the cross-shore transect off XUAN site in October 2015 (stratified condition) (**a**), January (well-mixed condition) (**b**), April (**c**) and June 2016 (weakly stratified condition) (**d**). The climatological discharge in the Ba Lat station (gray shade area) overlaid by the time evolution of the potential energy anomaly (PEA) index ϕ (**e**)

during the year and appears higher in winter by approximately half an order of magnitude (Fig. 5b, c). At the same time, the PCA-derived current ellipses did not exhibit noticeable changes in the tidal current magnitude between seasons. However, there were significant differences in the shape of the tidal ellipses under stratified and mixed conditions, revealing a large variability of the cross-shore tidal shear (Fig. 14). The HFR-derived velocities on October 18–25, 2015 and January 03–10, 2016 corresponding to the stratified and mixed conditions were selected for the assessment of the influence of the river discharge on the tidal current ellipses. Figure 14 demonstrates that the tidal current ellipses close to the XUAN radar site are flattened in January when the water is well mixed. On the contrary, the ellipses within roughly 40 km in the coastal zone are more circular in October and exhibit a greater tendency toward the cw motions (rotary coefficients range from 0.4 to 0.6). This phenomenon is called "tidal cross-shore straining" (Simpson and Sharples 2012).

To further investigate the role of freshwater discharge in the polarization of the tidal ellipses, we used the current profiles obtained from the AWAC meter in October 2015 (Fig. 15). During this highly stratified period, the coastal current is characterized by a two-layer circulation, with the surface flow detached from the bottom layer flow (Mazzini et al. 2014; Rogowski et al. 2019). The important feature of the tidal circulation is the difference in the current vector rotations between the surface and bottom layers (Fig. 15). Current vectors rotate cw in the surface layer (up to 6 m below the surface), with a corresponding r value of approximately −0.4, whereas in the lower half of the water column, the currents

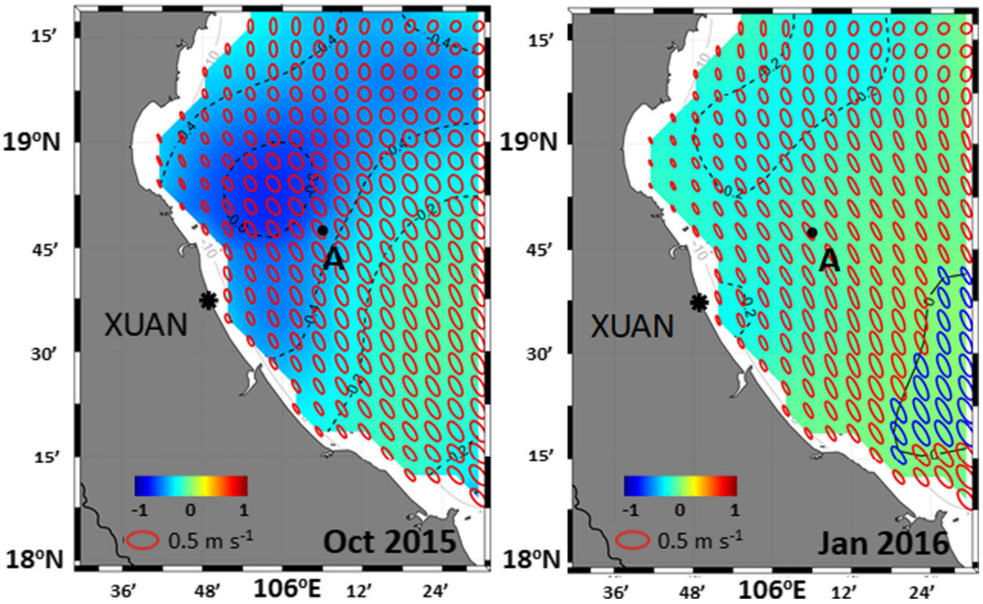

Fig. 14 PCA-derived tidal current ellipses, averaged during 7 days of spring tide in October 2015 (October 18–25, stratified condition) and in January 2016 (January 03–10, well-mixed condition). The rotary coefficient of tidal ellipses is shown by color shading. The current vector rotation is shown in blue for ccw and in red for cw rotating currents

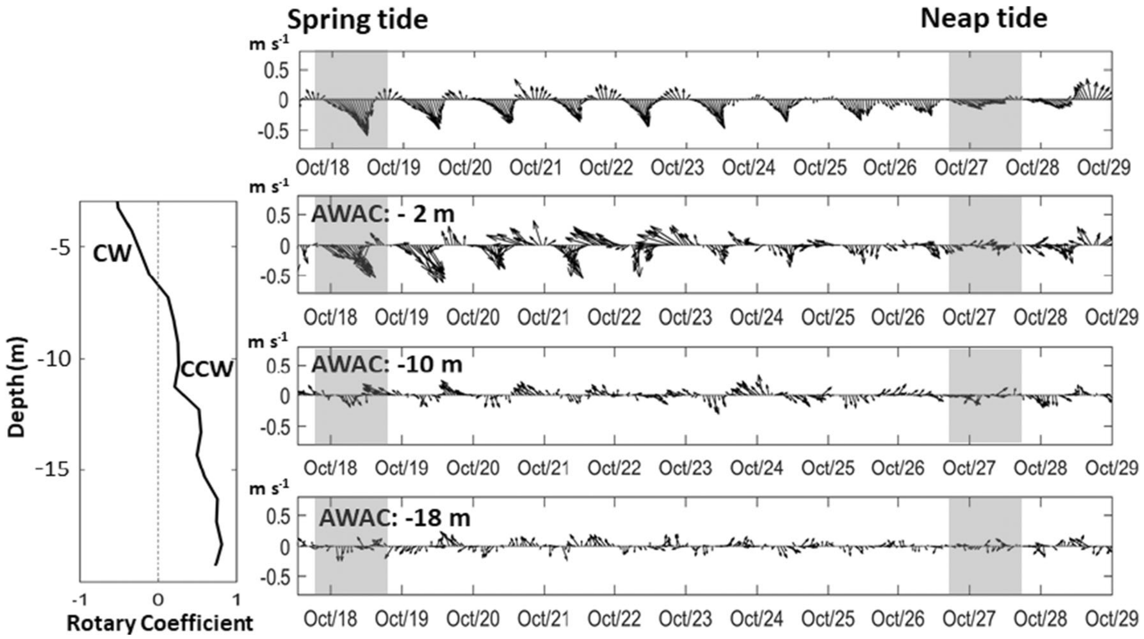

Fig. 15 Time series of HFR-derived current velocities and observed velocities at AWAC mooring location in October 2015 at different depth levels: surface layer (− 2 m), mid-depth (− 10 m), and bottom layer (− 18 m) (right). Vertical profile of the rotary coefficient from measured velocities (left). Gray shading shows the peak spring tide and neap tide periods

achieve a ccw rotation with $r > 0.6$. A separation between two layers is clearly observed at a depth of 7 m, as presented in Fig. 15 (left panel). The maximum current velocities in the surface layer (up to 6 m below the surface) vary from 0.3 m s^{-1} on the neap tide to 0.6 m s^{-1} on a spring tide, and the current direction matches the advection of the river plume along the coast. Lower velocities are observed below that depth, with maximum values ranging from 0.1 to 0.4 m s^{-1}. The current velocity profile is highly sheared and shows a direction reversal in certain periods (Fig. 15, right panel).

The spatial distribution of the rotary coefficients also indicates variations between stratified and mixed periods (Fig. 14). In the stratified period, due to the detachment of the surface layer from the less mobile bottom layer (trapped layer), the cw rotation is more pronounced (the rotary coefficient is about − 0.6). Under a well-mixed condition in January, the tides act in the whole water column, which results in more rectilinear current vectors. The rotary coefficients range from 0 to − 0.2, indicating a low clockwise rotation.

4 Discussion

The analysis reported in this paper is primarily based on the observation by HFR, which is located in the southern GoT. Two radar systems were selected for the analysis of the surface circulation in a region with complicated dynamics associated with the domination of the East Asian monsoon. HFR-derived currents were obtained at high resolution (6 km in a rectangular grid and 1-h time step) using the 2dVar-EOF method. The comparison of the HFR observations and the data from AWAC mooring yields a good correlation (0.7) with acceptable RMSE differences (less than 0.12 m s^{-1}). In our opinion, the variational interpolation of the HFR data (EOF/2dVar) applied to the radial velocity measurements in the GoT provides slightly better results compared with the OMA technique in this region (Table 1). A comparison of two interpolation techniques performed in Bodega Bays, USA (Yaremchuk and Sentchev 2009), supports our conclusion.

The tides in the GoT can be described as a progressive tidal wave propagating northward along the eastern coast (Hainan coast) and propagating southward along the western side (Vietnamese coast) (Nguyen et al. 2014). By analyzing the HFR-derived current in this study, we observed the propagation of the tidal wave more clearly. The tidal wave enters the gulf mainly through the southern entrance and bounds to the east (Hainan Island coast) as a progressive Kelvin wave under the Coriolis forcing effect. The energy of diurnal tides here is already stronger than the semi-diurnal tides (Zu et al. 2008; Chen et al. 2009; Nguyen et al. 2014). The length of the gulf (approximately 500 km) is comparable with the Rossby radius of deformation $\frac{\sqrt{gD}}{f}$, which yields a value of about 400 km (at a latitude of 19° N with a depth of 40 m). Subsequently, the Coriolis force affects the tidal propagation in the GoT. Within the gulf, the tidal wave propagates much slower than in the open ocean, and its energy partly dissipates due to the bottom friction. However, the slow propagation of the tidal wave and the basin geometry cause the diurnal tides to be resonant and reflected at the northern enclosure of the gulf. The tidal wave then behaves as a combination of the standing wave and progressive wave motions, which is balanced by the Coriolis force, and bounds to the Vietnamese coast in the west and exits the gulf. Consequently, this makes the anticlockwise propagation dominant while the tidal wave propagates along the coasts. The results of the PCA analysis of the current velocities derived from the radar measurements support this consideration.

The result from the tidal harmonic analysis in Section 3.2.2 revealed that tidal motions account for a large percentage of the overall velocity variability. The contribution of the tidal current velocity variability in the GoT is approximately 60%. Therefore, it could be deduced that the residual currents, which includes wind, buoyancy, and, to a minor extent, remote forcing, account for the remaining 40% of the total velocity variability in the GoT.

Seasonal differences in the tidal current amplitudes in summer have been documented by Ding et al. (2013). From the mooring data analysis, the authors revealed that both the diurnal and semi-diurnal tidal ellipse major axes in northern GoT are larger in summer. In our study, the tidal current ellipses provided by the PCA of the velocity measurements did not exhibit noticeable changes in the tidal current amplitude other than the “tidal cross-shore straining” phenomenon due to the stratification of the water column. At the same time, the spectral analysis of basin-wide average HFR-derived current velocities indeed reveals an increase in energy by roughly a half of an order of magnitude at the diurnal and semi-diurnal frequencies during winter. This is contradictory to the finding of Ding et al. (2013) in the northern gulf. The seasonal variability of the tidal currents could be due to the adjustment of the currents to the wind (i.e., sea breeze). In summer, under the effects of the wind, the spectral energy at the diurnal and semi-diurnal frequencies is found to be spread toward lower frequencies. The inertial motions in summer are more energetic due to persistent southwesterly wind in summer, indicating an adjustment of wind-driven currents to wind forcing (Fig. 5c). Contrarily, the inertial peak in the PSD of the currents in winter becomes less significant and shifts toward the sub-inertial band, implying that the inertial oscillations are insignificant during this period.

The large seasonal variability of sea surface currents is associated with the monsoon wind. Wind-driven currents largely contribute to the surface circulation variability in the GoT, as shown by the wind-current correlation analysis. During winter, the northeast wind drives the surface current onshore. In summer, the wind changes to the offshore direction, thus pushing the water offshore. The surface currents veer to the right of the wind, which is in agreement with the Ekman theory, and the water flow is directed eastward to the Hainan coast. The correlation coefficient of the wind and HFR-derived current is found to be high in winter and low in summer. Based on this analysis, we can conclude that the residual current in the southern gulf in winter is primarily generated by strong northeasterly wind. Typically, the response time of the current to the wind is slower under mixed conditions since the flux of the momentum from the atmosphere requires more time to be transferred vertically inside the water column (Dzwonkowski et al. 2009). The zero lag, which is found in the analysis of the wind-surface current correlation in winter, could be the result of the strong wind effect. In the middle of winter (December to January), strong northeasterly wind, which occasionally exceeds 0.1 N m^2, immediately drives the surface current. Contrary to mid-summer, the higher response time (6-h lag) of the surface current to the wind is observed when the freshwater is trapped at the mouth of the Red River (Table 2).

Our analyses revealed a cyclonic circulation structure in the southern gulf throughout the year. Considering the surface current magnitude, the average surface current velocities are generally larger during fall and winter under the effects of strong northeasterly wind than during summer and spring. Moreover, in our analyses, nearshore current velocities observed by HFR are often much larger than those in the middle gulf throughout the whole year. The southward coastal current along the coast is assumed to be a particular feature of the circulation pattern, which was demonstrated in the recent study of the GoT circulation by Rogowski et al. (2019). Also, Manh and Yanagi (2000) had shown that in summer, the tide-induced and density-driven currents have the same southward direction in the southern gulf.

The freshwater discharge from the Red River affects the coastal dynamics and increases the complexity of the current patterns. A portion of the plume in the surface layer (about 5 m thick) is detached from the bottom layer. The coastal current is described as a surface-advected river plume (Mazzini et al. 2014; Mulligan and Perrie 2019). The detached surface velocities are generally larger than those of the bottom layer (Fig. 15). Associated with the down-coast river plume, a frictionless water body, which is forced by the river flow and the strong northeasterly wind, is responsible for the intensification of the coastal current. We demonstrated that the seasonal variability of the nearshore-offshore currents (the coastal current intensity and the asymmetry in Fig. 11) is related to the coupling between wind forcing and freshwater input from rivers along the Vietnamese coast. The onshore flow induced by the NE wind (negative cross-shore velocity) contributes to the intensification of the coastal jet. However, wind forcing alone cannot account for the whole variation of the coastal flow.

The northeasterly wind drives the freshwater plume from the Red River southward during the end of summer to early winter, resulting in the high stratification of the region. Conversely, mixed conditions occur during mid-winter, which coincides with the minimum discharge from the Red River and cooler surface temperature. The large variability of cross-shore tidal shear in the coastal area is observed under stratified and mixed conditions in October and January, respectively. As the tide takes the form of a progressive Kelvin wave propagating parallel to the shoreline, the tidal currents are rectilinear. The stratification induced from the Red River plume modified the tidal current ellipses polarizations. During the stratified period, the cw rotation of the surface current vectors is enhanced while in the bottom layer, the current vectors rotate ccw. The horizontal tidal shear weakens when mixing occurs and is enhanced under stratified conditions. During mid-winter, the mixing increases due to the strong wind and surface waves, thus tightening the tidal ellipses. Schematically, the mean stratification under low-power-steering input (weaker wind) modifies the polarization of the tidal ellipses and generates a strong cross-shore tidal shear (Souza and Simpson 1996; Simpson and Sharples 2012).

Furthermore, the discharge from the Red River carries large quantities of nutrients and controls the interannual variation of nutrient supply along the coast of GoT (Chen et al. 2009; Loisel et al. 2017). Moreover, it provides large sediment flux into the gulf (Vinh et al. 2014). Knowledge of how freshwater interacts with the coastal circulation in this area and its variation is important to understand the coastal dynamics and thus requires thorough assessment in future studies.

5 Concluding remarks

The spatial and temporal variabilities of the surface circulation in the southern Gulf of Tonkin were assessed using the continuous velocity time series obtained by HFRs during the period of 2014–2016. The large length of the time series and spatial coverage by radar observations, resulting from the application of the variational approach of data processing (EOF/2dVar), enabled the characterization of the current variability spanning from the tidal and sub-tidal frequencies to the annual scale.

Spectral analysis of the velocity time series revealed a pronounced seasonal variability and an energy transfer from large-scale (low-frequency) variability in winter to low-scale (higher frequency) variability in summer. For instance, the wind-induced variability of the surface currents at the diurnal frequency was found to be amplified in summer. The temporal variability of the kinetic energy of the surface currents was found to be tightly correlated with the wind forcing variations.

Our analyses revealed that tidal motions account for a large percentage of surface current variability in the GoT, which is approximately 60% of the overall surface velocity variability. Stratification induced by freshwater input from the Red River affects the tidal currents by modifying the polarization of the tidal ellipses. Moreover, it generates tidal straining within a wide (~ 40 km) coastal region located south of the Red River mouth.

The coastal flow is a prominent feature of the general circulation in the southern GoT. Its width, strength, and mode of variability are largely governed by a combination of freshwater input and wind forcing, particularly the cross-shore wind component. Remote forcing can also affect the coastal current variability, as suggested by Rogowski et al. (2019). However, we did not capture its effect on our observation-based study. The annual variability of the coastal current does not follow a seasonal cycle. The stage of current intensification lasts 8 to 9 months, with larger velocities and seaward extension observed in late fall (September to October) and weaker current (lower velocities) occurring in mid-summer (June to July). It was found that the monsoon atmospheric circulation contributes to the temporal variations of the coastal flow in two ways. The zonal wind component experiences a closely harmonic seasonal variability and induces the cross-shore mass exchange, thus affecting the coastal flow speed and seaward extension. Contrarily, the meridional (along shore) wind component causes a weak modulation of the along-shore current. The Red River discharge, which is characterized by bimodal temporal evolution, affects the coastal current variability and enhances the asymmetry in the current velocity variations.

The obtained data and the results from the database analysis are thought to be useful for further studies of coastal circulation in the GoT, i.e., for the improvement of numerical models and for practical applications related to marine biology, ocean color remote sensing, Search and Rescue (SaR) operations, and management of the marine environment.

Acknowledgments This study was supported by the University of Littoral Côte d'Opale and the Région "Hauts-de-France" PhD fellowship. The study was also partly supported by the Vietnam state-level project KC09.14/16-20. The data set used in this study has been collected in the framework of the US-Vietnam collaboration project: "Gulf of Tonkin Circulation study" (NICOP N62909-15-1-2018), financed by the Office of Naval Research (ONR). We also thank the field team of the CFO for technical assistance. We appreciate the valuable comments from two anonymous reviewers for helping in improving the paper.

Authors' contributions M.C.T. performed the data analysis and wrote the original version of the manuscript. A.S. proposed the ideas and was deeply involved in the analysis, manuscript organization, and co-writing. K.C.N. gave valuable comments and revised the manuscript.

Funding This study was funded by Université du Littoral-Côte d'Opale for PhD scholarship fellowship and partly supported by Vietnam state-level project KC09.14/16-20.

Compliance with ethical standards

Conflict of interest The authors declare that they have no conflict of interest.

References

Bassin CJ, Washburn L, Brzezinski M, McPhee-Shaw E (2005) Submesoscale coastal eddies observed by high frequency radar: a new mechanism for delivering nutrients to kelp forests in the Southern

California Bight. Geophys Res Lett 32(12). https://doi.org/10.1029/2005GL023017

Beardsley RC, & Rosenfeld LK (1981) Introduction to the CODE-1 moored array and large-scale data report, in CODE-1: Moored Array and Large-Scale Data Report

Chen C, Gao G, Qi J, Proshutinsky A, Beardsley RC, Kowalik Z, Lin H, Cowles G (2009) A new high-resolution unstructured grid finite volume Arctic Ocean model (AO-FVCOM): an application for tidal studies. J Geophys Res Oceans 114(C8). https://doi.org/10.1029/2008JC004941

Chen C, Lai Z, Beardsley RC, Xu Q, Lin H, Viet NT (2012) Current separation and upwelling over the southeast shelf of Vietnam in the South China Sea. J Geophys Res Oceans 117(C3). https://doi.org/10.1029/2011JC007150

Chern C-S, Jan S, Wang J (2010) Numerical study of mean flow patterns in the South China Sea and the Luzon Strait. Ocean Dyn 60(5):1047–1059. https://doi.org/10.1007/s10236-010-0305-3

Ding Y, Chen C, Beardsley RC, Bao X, Shi M, Zhang Y, Lai Z, Li R, Lin H, Viet NT (2013) Observational and model studies of the circulation in the Gulf of Tonkin, South China Sea. J Geophys Res Oceans 118(12):6495–6510. https://doi.org/10.1002/2013JC009455

Dzwonkowski B, Kohut JT, Yan X-H (2009) Sub-inertial characteristics of the surface flow field over the shelf of the central Mid-Atlantic Bight. Cont Shelf Res 29(15):1873–1886. https://doi.org/10.1016/j.csr.2009.07.005

Fujii S, Heron M, Kim K, Lai J-W, Lee S-H, Wu X, Wu X, Wyatt L, Yang W-C (2013) An overview of developments and applications of oceanographic radar networks in Asia and Oceania countries. Ocean Sci J 48:69–97. https://doi.org/10.1007/s12601-013-0007-0

Furgerot L, Sentchev A, Bailly du Bois P, Lopez G, Morillon M, Poizot E, Méar Y, Bennis AC (2020) One year of measurements in Alderney Race: preliminary results from database analysis. Phil Trans R Soc A 378(2178):20190625

Gan J, Li H, Curchitser EN, Haidvogel DB (2006) Modeling South China Sea circulation: response to seasonal forcing regimes. J Geophys Res Oceans 111(C6). https://doi.org/10.1029/2005JC003298

Gao J, Xue H, Chai F, Shi M (2013) Modeling the circulation in the Gulf of Tonkin, South China Sea. Ocean Dyn 63(8):979–993. https://doi.org/10.1007/s10236-013-0636-y

Gao JS, Chen B, Shi MC (2015) Summer circulation structure and formation mechanism in the Beibu Gulf. Sci China Ser D-Earth Sci 58:286–299

Gao J, Wu G, Ya H (2017) Review of the circulation in the Beibu Gulf, South China Sea. Cont Shelf Res 138:106–119. https://doi.org/10.1016/j.csr.2017.02.009

IMHEN & UNDP (2015) Vietnam special report on managing the risks of extreme events and disasters to advance climate change adaptation (VN-SREX). Website: http://www.imh.ac.vn/. ISBN 978-604-904-623-0

Kaplan DM, Lekien F (2007) Spatial interpolation and filtering of surface current data based on open-boundary modal analysis. J Geophys Res Oceans 112(C12). https://doi.org/10.1029/2006JC003984

Kim SY, Terrill EJ, Cornuelle BD (2008) Mapping surface currents from HF radar radial velocity measurements using optimal interpolation. J Geophys Res Oceans 113(C10). https://doi.org/10.1029/2007JC004244

Kundu PK (1976) Ekman veering observed near the ocean bottom. J Phys Oceanogr 6(2):238–242. https://doi.org/10.1175/1520-0485(1976)006<0238:EVONTO>2.0.CO;2

Large WG, Pond S (1981) Open Ocean momentum flux measurements in moderate to strong winds. J Phys Oceanogr 11(3):324–336. https://doi.org/10.1175/1520-0485(1981)011<0324:OOMFMI>2.0.CO;2

Liu FS, Yu TC (1980) Preliminary study on the oceanic circulation in Beibu Bay. Trans Oceanol Limnol 1, 9–15, (in Chinese with English abstract)

Liu Y, Weisberg RH, Merz CR (2014) Assessment of CODAR SeaSonde and WERA HF radars in mapping surface currents on the West Florida Shelf. J Atmos Ocean Technol 31(6):1363–1382. https://doi.org/10.1175/JTECH-D-13-00107.1

Loisel H, Vantrepotte V, Ouillon S, Ngoc DD, Herrmann M, Tran V, Mériaux X, Dessailly D, Jamet C, Duhaut T, Nguyen HH, Van Nguyen T (2017) Assessment and analysis of the chlorophyll-a concentration variability over the Vietnamese coastal waters from the MERIS ocean color sensor (2002–2012). Remote Sens Environ 190:217–232. https://doi.org/10.1016/j.rse.2016.12.016

Lopez G, Bennis A-C, Barbin Y, Sentchev A, Benoit L, Marié L (2020) Surface currents in the Alderney race from high-frequency radar measurements and three-dimensional modelling. Philos Trans R Soc A Math Phys Eng Sci 378(2178):20190494. https://doi.org/10.1098/rsta.2019.0494

Manh D-V, Yanagi T (2000) A study on residual flow in the Gulf of Tongking. J Oceanogr 56(1):59–68. https://doi.org/10.1023/A:1011162524466

Mazzini PLF, Barth JA, Shearman RK, Erofeev A (2014) Buoyancy-driven coastal currents off Oregon during fall and winter. J Phys Oceanogr 44(11):2854–2876. https://doi.org/10.1175/JPO-D-14-0012.1

Mulligan RP, Perrie W (2019) Circulation and structure of the Mackenzie River plume in the coastal Arctic Ocean. Cont Shelf Res 177:59–68. https://doi.org/10.1016/j.csr.2019.03.006

Nguyen NM, Patrick M, Florent L, Sylvain O, Gildas C, Damien A, Van Uu D (2014) Tidal characteristics of the gulf of Tonkin. Cont Shelf Res 91:37–56. https://doi.org/10.1016/j.csr.2014.08.003

Paduan JD, Washburn L (2013) High-frequency radar observations of ocean surface currents. Annu Rev Mar Sci 5(1):115–136. https://doi.org/10.1146/annurev-marine-121211-172315

Pawlowicz R, Beardsley B, Lentz S (2002) Classical tidal harmonic analysis including error estimates in MATLAB using T_TIDE. Comput Geosci 28(8):929–937. https://doi.org/10.1016/S0098-3004(02)00013-4

Piton V, Herrmann M, Lyard F, Marsaleix P, Duhaut T, Allain D, Ouillon S (2020) Sensitivity study on the main tidal constituents of the Gulf of Tonkin by using the frequency-domain tidal solver in T-UGOm. Geosci Model Dev 13(3):1583–1607. https://doi.org/10.5194/gmd-13-1583-2020

Rogowski P, Zavala-Garay J, Shearman K, Terrill E, Wilkin J, Tran HL (2019) Air-sea-land forcing in the Gulf of Tonkin: assessing seasonal variability using modern tools. Oceanography 32(2):150–161

Sentchev A, Forget P, Barbin Y (2009) Residual and tidal circulation revealed by VHF radar surface current measurements in the southern Channel Isles region (English Channel). Estuar Coast Shelf Sci 82(2):180–192. https://doi.org/10.1016/j.ecss.2008.12.003

Sentchev A, Forget P, Barbin Y, Yaremchuk M (2013) Surface circulation in the Iroise Sea (W. Brittany) from high resolution HF radar mapping. J Mar Syst 109–110:S153–S168. https://doi.org/10.1016/j.jmarsys.2011.11.024

Simpson JH, Sharples J (2012) Introduction to the physical and biological oceanography of shelf seas. Cambridge University Press, Cambridge Core. https://doi.org/10.1017/CBO9781139034098

Simpson JH, Brown J, Matthews J, Allen G (1990) Tidal straining, density currents, and stirring in the control of estuarine stratification. Estuaries 13(2):125–132. https://doi.org/10.2307/1351581

Souza AJ, Simpson JH (1996) The modification of tidal ellipses by stratification in the Rhine ROFI. Cont Shelf Res 16(8):997–1007. https://doi.org/10.1016/0278-4343(95)00042-9

Stewart RH, Joy JW (1974) HF radio measurements of surface currents. Deep-Sea Res Oceanogr Abstr 21(12):1039–1049. https://doi.org/10.1016/0011-7471(74)90066-7

Thiébaut M, Sentchev A (2017) Asymmetry of tidal currents off the W.Brittany coast and assessment of tidal energy resource around the Ushant Island. Renew Energy 105:735–747. https://doi.org/10.1016/j.renene.2016.12.082

Vinh, V. D., Ouillon, S., Thanh, T. D., & Chu, L. V. (2014). Impact of the Hoa Binh dam (Vietnam) on water and sediment budgets in the Red River basin and delta. Hydrology and Earth System Sciences, 18(10), 3987–4005. https://doi.org/10.5194/hess-18-3987-2014

Yaremchuk M, Sentchev A (2009) Mapping radar-derived sea surface currents with a variational method. Cont Shelf Res 29(14):1711–1722. https://doi.org/10.1016/j.csr.2009.05.016

Yaremchuk M, Sentchev A (2011) A combined EOF/variational approach for mapping radar-derived sea surface currents. Cont Shelf Res 31(7–8):758–768. https://doi.org/10.1016/j.csr.2011.01.009

Ye AL, Robinson IS (1983) Tidal dynamics in the South China Sea. Geophys J Int 72(3):691–707. https://doi.org/10.1111/j.1365-246X.1983.tb02827.x

Yoshikawa Y, Matsuno T, Marubayashi K, Fukudome K (2007) A surface velocity spiral observed with ADCP and HF radar in the Tsushima Strait. J Geophys Res Oceans 112(C6). https://doi.org/10.1029/2006JC003625

Zu, T., Gan, J., & Erofeeva, S. Y. (2008). Numerical study of the tide and tidal dynamics in the South China Sea. Deep Sea Research Part I: Oceanographic Research Papers, 55(2), 137–154. https://doi.org/10.1016/j.dsr.2007.10.007